

---

**RESEARCH ARTICLE**

# YNetr: Dual-Encoder architecture on Plain Scan Liver Tumors (PSLT)

Wen Sheng<sup>1\*</sup> | Zhong Zheng<sup>1\*</sup> | Jiajun Liu<sup>3</sup> | Han Lu<sup>2</sup> | Hanyuan Zhang<sup>2</sup> | Zhengyong Jiang<sup>2</sup> | Zhihong Zhang<sup>1</sup> | Daoping Zhu<sup>1</sup>

<sup>1</sup>Gong'an County People's Hospital, Hubei, China

<sup>2</sup>Xi'an Jiaotong-Liverpool University, Jiangsu, China

<sup>3</sup>Beijing University of Posts and Telecommunications, Beijing, China

## Correspondence

Zhengyong Jiang, Xi'an Jiaotong-Liverpool University.  
Email:zhengyong.jiang02@xjtlu.edu.cn

Zhihong Zhang, Gong'an County People's Hospital  
Email:27573920@qq.com

Daoping Zhu, Gong'an County People's Hospital  
Email: zhudaoping@163.com

## Funding information

This research was funded by the Suzhou Science and Technology Project (SYG202122), the Research Development Fund of XJTLU (RDF-19-02-23) and Suzhou Municipal Key Laboratory for Intelligent Virtual Engineering (SZS2022004).

**Background:** Liver tumors are abnormal growths in the liver that can be either benign or malignant, with liver cancer being a significant health concern worldwide. However, there is no dataset for plain scan segmentation of liver tumors, nor any related algorithms. To fill this gap, we propose Plain Scan Liver Tumors(PSLT) and YNetr.

**Methods:** A collection of 40 liver tumor plain scan segmentation datasets was assembled and annotated. Concurrently, we utilized Dice coefficient as the metric for assessing the segmentation outcomes produced by YNetr, having advantage of capturing different frequency information.

**Results:** The YNetr model achieved a Dice coefficient of 62.63% on the PSLT dataset, surpassing the other publicly available model by an accuracy margin of 1.22%. Comparative evaluations were conducted against a range of models including UNet 3+, XNet, UNetr, Swin UNetr, TransBTS, COTr, nnUNetv2 (2D), nnUNetv2 (3D fullres), MedNext (2D) and MedNext(3D fullres).

**Conclusions:** We not only proposed a dataset named PSLT (Plain Scan Liver Tumors), but also explored a structure called YNetr that utilizes wavelet transform to extract different frequency information, which having the SOTA in PSLT by experiments.

## KEYWORDS

plain scan liver tumors dataset, segmentation, artificial intelligence, dual-encoder, wavelet

# 1 | INTRODUCTION

## 1.1 | Background

Computed Tomography (CT) is a diagnostic technique that uses precisely collimated X-ray beams and highly sensitive detectors to perform sectional scans around a specific part of the human body. This method is characterized by its rapid scanning time and clear images. It can be applied to scan various parts of the body and holds immense clinical value for disease diagnosis. CT scans are increasingly used for abdominal diseases, primarily for diagnosing conditions related to the liver, gallbladder, pancreas, spleen, peritoneal cavity, retroperitoneal space, and the urinary and reproductive systems. They are particularly useful for diagnosing space-occupying lesions, inflammatory, and traumatic changes.

Liver tumors refer to neoplasms occurring in the liver, which can be benign or malignant. Malignant liver tumors mainly include primary and secondary liver cancers, along with other malignancies like hepatoblastoma and sarcoma. Benign liver tumors include hemangioma, adenoma, and focal nodular hyperplasia.

Various diagnostic methods are available for liver tumors, such as ultrasound, CT, MRI, and even PET-CT. Currently, CT is the most widely used due to its ability to display liver cross-sections every 0.5-1 cm, avoiding overlap from different angles of the liver. This technique reveals tumors and lesions within the liver, including their location, size, shape, and relationship with surrounding tissues. CT enhancement is performed for further clarification when the nature of a lesion is difficult to determine.

In the medical field, when a patient exhibits liver function abnormalities, employing CT scanning to determine the type of liver disease is crucial. However, with the increasing workload on physicians, manually identifying liver tumors using visual inspection is extremely time-consuming. To save diagnostic time, doctors can utilize artificial intelligence to segment lesions, aiding in diagnosis. Particularly in an era where deep learning is rapidly advancing, the effectiveness of artificial intelligence has been notably demonstrated. This has further

propelled the application of artificial intelligence in medical imaging diagnostics.

## 1.2 | Motivation

However, in existing studies, all research on liver tumor segmentation is based on contrast-enhanced CT liver tumor segmentation, with the LiTS [1] dataset and related algorithms (such as nnU-Net [2]) being prominent examples. Despite this, research on plain scan CT liver tumor segmentation remains limited, even though it holds clinical significance. Specifically, the clinical significance of plain scan CT liver tumor segmentation includes:

- **Advantage of Avoiding Contrast Agents:** Contrast-enhanced CT scans typically require iodine-based contrast agents, which can pose risks for certain patients (such as those with iodine allergies or renal insufficiency). Plain scan CT, as a diagnostic method that does not require contrast agents, is a safer choice for these patients.
- **Cost-Effectiveness and Accessibility:** Compared to enhanced scans, plain scan CT is generally less expensive and simpler to operate. In resource-limited areas (such as primary care hospitals) or in emergency situations, plain scan CT might be a more practical or faster option.
- **Early Detection and Monitoring:** When the patients exhibit no obvious symptoms, plain scan CT can be used for early detection and monitoring of liver tumors.

Furthermore, developing algorithms capable of accurately identifying liver tumors from plain scan CT images demonstrates the progress of artificial intelligence and machine learning in the field of medical imaging. This could pave the way for future medical imaging analysis technologies.

From the perspective of existing semantic segmentation models, most models have only one branch as an encoder and one branch as a decoder. In contrast, XNet [3] uses two branches as encoders and two branches as decoders to capture features at different frequencies of

the image and adjust outputs for semi-supervised segmentation. However, XNet still has its drawbacks:

- **Decoder Branch Redundancy:** XNet uses two branches as decoders, but studies have shown that the outputs of XNet’s two branches are very similar. Therefore, it is necessary to merge the two decoder branches of XNet into one through feature fusion. Meanwhile, in semi-supervised tasks, using two decoders is justifiable because it allows for the comparison and adjustment of the outputs from both decoders to accommodate unlabeled data. However, in fully supervised tasks, employing two decoders is unreasonable. This is because the labels are already known, eliminating the need for additional adjustments.
- **Feature Extraction Limitations:** XNet solely relies on CNNs for feature extraction, which cannot capture long-term dependencies. To address this issue, considering the use of transformers as feature extractors is necessary.

### 1.3 | Key Contribution

To address these issues, we have developed the first plain scan liver tumor segmentation dataset, PSLT (Plain Scan Liver Tumors). Additionally, we introduced a model, YNetr, featuring two branches as encoders and one branch as a decoder. This model achieved a Dice coefficient of 62.63%(SOTA) on our dataset. In summary, our contributions are as follows:

- **PSLT (Plain Scan Liver Tumors):** To address the gap in plain scan liver tumor segmentation datasets, we have developed the first dedicated dataset for this purpose, PSLT (Plain Scan Liver Tumors). It encompasses plain scan data from forty distinct patients, totaling 10,923 slices.
- **Novel Model YNetr:** We propose a novel model, YNetr, which employs a dual-branch architecture as encoders for multi-level feature extraction and a singular branch as a decoder for feature fusion. Additionally, the vision transformer [4] architecture, mir-

roring the UNETR [5] structure, is utilized within the encoder to capture global features of images. The conclusive experimental results demonstrate that YNetr achieves state-of-the-art (SOTA) performance on the PSLT dataset.

The rest of the paper is organized as follows: In Section 2, the specific content of PSLT and the structure of YNetr will be mentioned. In Section 3, the results of the experiments will be covered. In Section 4, we will discuss the existing liver tumor datasets and some segmentation methods, and the advantages of the PSLT dataset compared to these will also be mentioned. In Section 5, we will address the challenges of the PSLT dataset. Finally, in Section 6, we will summarize the paper and provide directions for future research.

## 2 | METHODS

### 2.1 | Proposed Dataset PSLT

#### 2.1.1 | Dataset Summary

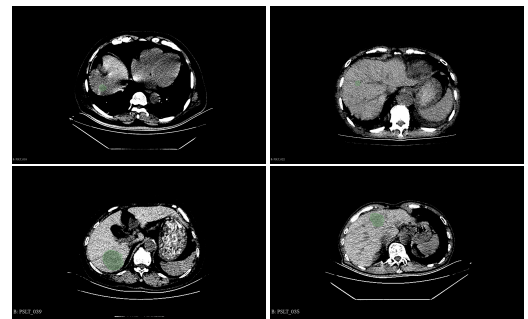


**FIGURE 1** Four examples of PSLT, the green label represents liver tumor

The PSLT dataset consists of forty plain scan 3D CT volumes collected from forty distinct patients by Gong’an County People’s Hospital, Hubei Province. This dataset includes a wide variety of cases such as abdominal scans, thoracoabdominal scans, tumors in different stages. Each volume was comprehensively scanned utilizing a SIEMENS CT scanner, ensuring consistent imaging quality. The volumes span an extensive range, en-

**TABLE 1** Comparison of various datasets for liver tumor segmentation.

Dataset	Plain Scan	Liver Tumor	Segmentation	Volume Number	Modality
TCGA-LIHC [6]	×	✓	×	1688	CT, MR, PT
SILVER07 [7]	×	×	✓	30	CT
LTSC'08 [7]	×	✓	✓	30	CT
VISCERAL'16 [8]	×	×	✓	60/60	CT/MRI
CHAOS19 [9]	×	×	✓	40/120	CT/MRI
LiTS [1]	×	✓	✓	201	CT
<b>PSLT(Ours)</b>	✓	✓	✓	40	CT

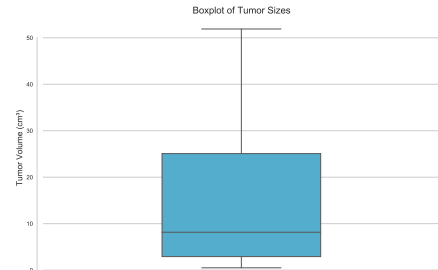
compassing 145 to 873 slices per volume, with each slice boasting a resolution of 512x512 pixels. This evidences the remarkable high-resolution nature of the PSLT dataset. While each volume uniformly includes liver imagery, the scanned regions exhibit considerable variation, including abdominal and thoracoabdominal scans as Table 2. This heterogeneity considerably enriches the dataset's diversity, offering a robust basis for various analytical applications. Four illustrative example

	abdominal	Thoracoabdominal
Trainset ( $n = 28$ )	20	8
Testset ( $n = 12$ )	8	4

**TABLE 2** Scan site in PSLT

from the PSLT dataset is showcased in Figure 1. To ensure patient confidentiality, all data were subjected to rigorous anonymization processes and received the necessary ethical committee approvals, thereby upholding stringent privacy standards. For research and development purposes, the PSLT dataset was partitioned into two subsets randomly: a training set consisting of 28 volumes (7667 slices) and a testing set comprising 12 volumes (3256 slices), as delineated in Table 3. We also show the size distribution of liver tumors in Figure 2. This indicates that half of the tumors range between 3 cubic centimeters and 25 cubic centimeters, with a more frequent distribution of smaller tumors below 8 cubic centimeters. The prevalence of these smaller tu-

mors under 8 cubic centimeters adds complexity to the identification of lesions.

**FIGURE 2** Size distribution of liver tumor

	Total slices	Max slices	Min slices
Trainset ( $n = 28$ )	7667	873	571
Testset ( $n = 12$ )	3256	145	169

**TABLE 3** The Slice Distribution in PSLT

### 2.1.2 | Professional data annotation

Due to the complexity of three-dimensional medical imaging data, manually annotating each frame of 3D medical images is extremely time-consuming. To enhance the efficiency of annotation, we employed semi-automated techniques using the 3D Slicer software [10].

Specifically, a chief physician with over 10 years of experience conducted the initial annotations using 3D Slicer. Subsequently, these annotations were reviewed by a deputy chief physician with more than 20 years of experience. In cases of differing opinions, a consensus was reached through discussions involving multiple colleagues. The data labeling task will continue until the doctors believe there are no issues. During the annotation phase, each volume required 0.3-0.5 hours for annotation by the chief physician and 0.05-0.2 hours for review by the deputy chief physician, including discussions. Overall, approximately three months were invested in the collection, annotation, and review of the PSLT dataset.

### 2.1.3 | Comparison to Other datasets

Compared to existing datasets, our dataset is the first to focus on non-contrast CT scans for liver tumor segmentation. A comparative analysis with other datasets is presented in Table 1, illustrating its unique position in the current research landscape.

## 2.2 | Proposed Model YNetr

### 2.2.1 | Framework Overview

The YNetr architecture features a Y-shaped structure, as depicted in Figure 5. It comprises two branches forming the encoder and a single branch as the decoder. Each branch utilizes the structure of UNETR. Within the encoder, a 1D sequence is generated from a three-dimensional input volume  $x \in \mathbb{R}^{(H \times W \times D \times C)}$ , where (H, W, D) represents the height, width and depth, and C denotes the input channels. This sequence is formed by flattening uniformly non-overlapping patches  $x_v \in \mathbb{R}^{(N \times (P^3 \cdot C))}$ , where (P, P, P) indicates the dimensions of a patch and  $N = (H \times W \times D) / P^3$  represents the length of the sequence. Different from the UNETR framework, the YNetr architecture innovatively utilizes a dual-branch encoder to capture medical imaging data across varied frequencies. In a distinctive approach to integrating encoder and decoder information, YNetr employs

addition as its fusion technique, instead of the more conventional method of dimensional stacking. This design choice facilitates a more seamless and effective integration of multi-scale features by capturing different frequency information, enhancing the model's capacity to process complex medical images.

### 2.2.2 | Wavelet Transform

In the realm of 3D medical imaging, data fundamentally represents discrete signals encompassing information across various frequencies. The wavelet transform is adept at segregating this multi-frequency information effectively. This transformation is applied to partition raw image data into distinct components, namely low frequency (LF), and high frequency (HF) in three orientations: horizontal, vertical, and diagonal. These are technically denoted as R (raw image) for LF. H, V, and D are denoted for horizontal, vertical, and diagonal HF components, respectively. These components capture the low-frequency signals along with high-frequency information in different orientations. For the comprehensive representation of high-frequency data, it is essential to amalgamate these directional high-frequency components. The formulation of low and high-frequency information is delineated as follows:

$$LF = R \quad (1)$$

$$HF = H + V + D \quad (2)$$

where the low-frequency information is characterized by reduced noise and fewer details, enhancing the clarity of the overarching structure. In contrast, the high-frequency information provides more noise but clearer object boundaries, as depicted in the accompanying figure as shown in Figure 3 and Figure 4.

### 2.2.3 | Details of YNetr

To capture the global information of an image, each branch of the encoder incorporates twelve layers of the

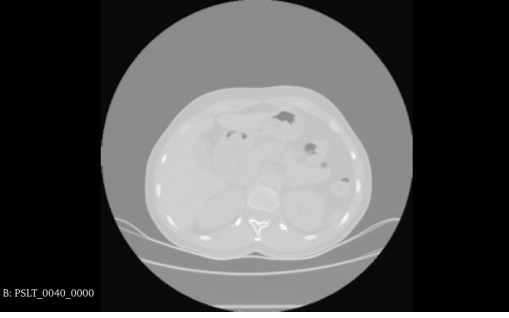


**FIGURE 3** Low frequency

UNetr block. Specifically, at the 3rd, 6th, 9th, and 12th layers, outputs are generated with dimensions of  $\frac{H}{16} \times \frac{W}{16} \times \frac{D}{16} \times 768$  by unfolding. In other layers of the encoder, the output will be taken as the input for the next layer in the form of  $N \times (P^3 \cdot C)$  where  $N = (H \times W \times D)/P^3$ ,  $P = 16$  and  $C = 768$ . Post convolution, these dimensions are transformed to  $\frac{H}{8} \times \frac{W}{8} \times \frac{D}{8} \times 512$ ,  $\frac{H}{8} \times \frac{W}{8} \times \frac{D}{8} \times 512$ ,  $\frac{H}{4} \times \frac{W}{4} \times \frac{D}{4} \times 256$ , and  $\frac{H}{2} \times \frac{W}{2} \times \frac{D}{2} \times 128$  respectively. During the decoder phase (the central line in Figure 5), convolutional operations are applied for upsampling to restore the image to its original size. Additionally, given that the model incorporates two encoders but only a single decoder, we opt for additive fusion rather than dimensional stacking for skip connections, thereby integrating the encoder information into the decoder. Figure 6 presents the topological flow chart of YNetr.

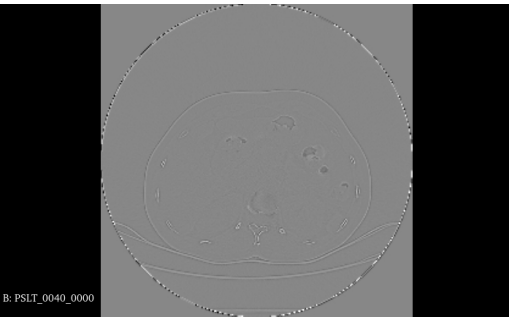


**FIGURE 4** High frequency

## 2.3 | Loss Function

In our experiments, the loss function is crucial for guiding the segmentation task towards optimal performance. We have employed a combined Dice and cross-entropy (CE) loss function. This hybrid loss function leverages the advantages of both the Dice loss, which is proficient in handling class imbalance by measuring overlap, and the CE loss, which robustly penalizes incorrect predictions on a voxel-wise basis. The formulation of our adopted loss function is as follows:

$$L_{\text{Dice-CE}}(G, Y) = \alpha L_{\text{Dice}}(G, Y) + (1 - \alpha) L_{\text{CE}}(G, Y) \quad (3)$$

where  $G$  represents the ground truth and  $Y$  denotes the predicted segmentation. The parameter  $\alpha$  strikes a balance between the two loss components. In this case, we define  $\alpha$  as  $\frac{1}{2}$  by experiments. Specifically, the Dice loss  $L_{\text{Dice}}$  is defined by:

$$L_{\text{Dice}}(G, Y) = 1 - \frac{2 \sum_i G_i Y_i}{\sum_i G_i + \sum_i Y_i} \quad (4)$$

and the cross-entropy loss  $L_{\text{CE}}$  is given by:

$$L_{\text{CE}}(G, Y) = - \sum_i G_i \log(Y_i) \quad (5)$$

Here,  $i$  indexes over all voxels,  $G_i$  denotes the ground truth value, and  $Y_i$  represents the predicted probability for each voxel.

## 2.4 | Evaluation Metrics

The evaluation of segmentation models is pivotal to our study. To quantitatively assess the performance of our proposed model, we employ the Dice coefficient, a widely recognized metric for segmentation tasks. The Dice coefficient, also known as the Dice similarity index, measures the overlap between the predicted segmentation and the ground truth. It is particularly effective for medical image segmentation where binary classification predominates. The Dice coefficient is mathematically defined as:

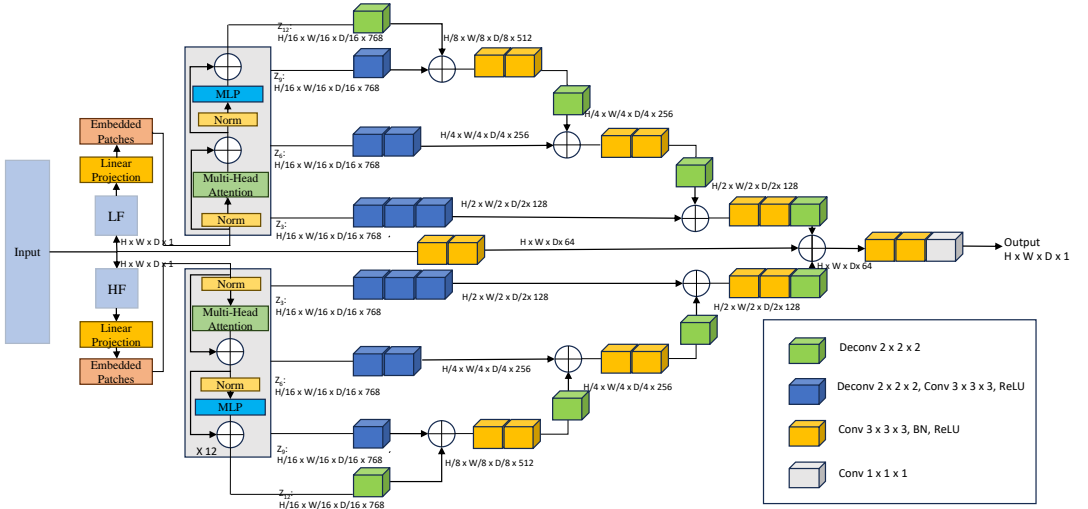


**FIGURE 5** Overview of YNetr architecture. The model employs Wavelet Transform to extract image information across various frequencies. Subsequently, it utilizes the fundamental architecture of UNETR, incorporating dual branches as encoders to extract features. Finally, it integrates this information through a sophisticated fusion process.

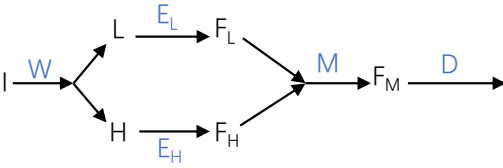


**FIGURE 6** Topological flow chart of segmentation process.

$$D(G, Y) = \frac{2 \times TP}{2 \times TP + FP + FN} \quad (6)$$

where  $G$  stands for the ground truth binary mask,  $Y$  signifies the predicted segmentation mask, TP denotes true positives, FP false positives, and FN false negatives.

## 2.5 | Implementation Details

The implementation of our YNetr model was conducted utilizing the PyTorch framework alongside MONAI, a medical open network for AI, which provided a robust

and flexible platform for our deep learning architecture. We used four NVIDIA GeForce RTX 3090 graphics cards for training. The model optimization was carried out using the AdamW optimizer, with the initial learning rate set at 0.0001 and the training carried out for over 300 epochs.

Within the encoder module, the patch resolution was calibrated to a  $16 \times 16 \times 16$  matrix. During the inference stage, a sliding window approach was employed, and the overlap rate was methodically set to 0.5 to ensure comprehensive coverage and accuracy. Here, the data were segmented into slices of  $128 \times 128 \times 128$  and subsequently fed into the model. To circumvent the model's propensity to learn excessively from the background, we maintained a balanced ratio of positive to negative samples at 1:1. Additionally, to mitigate central bias, random translations of  $48 \times 48 \times 48$  blocks were implemented.

Our conclusive experiments revealed that our model achieved a Dice coefficient precision of 62.63%, surpassing the performance of models in other comparative studies.

## 3 | RESULTS

### 3.1 | Comparative Experiments

In our comparative experiments in Table 4, several models were deployed to assess their performance: UNet 3+ [11], XNet [3], UNetr [5], Swin UNetr [12], TransBTS [13], COTr [14], nnUNetv2 (2D), nnUNetv2 (3D Fullres) [2], MedNext (2D), and MedNext (3D Fullres) [15]. Among these, Mednext (3D Fullres) had superior performance, achieving a Dice score of 61.41%. However, our model excelled by attaining a Dice coefficient accuracy of 62.63%, thereby surpassing the existing model MedNext (3D Fullres) which stood at 61.41%. The data from the comparative experiments are delineated in the table below.

**TABLE 4** Comparative Experiment Results, "bold" signifies SOTA performance

Model	Dice Coefficient (%)
UNet 3+	58.43
XNet	54.56
UNetr	58.67
Swin UNetr	58.89
TransBTS	55.64
COTr	56.72
nnUNetv2 (2D)	44.31
nnUNetv2 (3D Fullres)	60.21
MedNext (2D)	46.98
MedNext (3D Fullres)	61.41
<b>YNetr(Our Model)</b>	<b>62.63</b>

In Figure 7, we present a comparative segmentation illustration on the PSLT dataset between MedNext and YNetr. The visual comparison clearly demonstrates the superior segmentation efficacy of YNetr over MedNext, as evidenced by the enhanced delineation of the segmented regions.

## 3.2 | Ablation

### 3.2.1 | Patch Size

In our research, we empirically established a correlation between the patch size and the accuracy of the segmentation results. Specifically, our experiments demonstrate that: as the patch size increases, there is a corresponding decrease in segmentation accuracy which is shown in Figure 5. For instance, with a patch size set to  $16 \times 16 \times 16$ , our model achieved a Dice coefficient of 62.63%. In contrast, increasing the patch size to  $32 \times 32 \times 32$  resulted in a lower Dice coefficient of 61.08%.

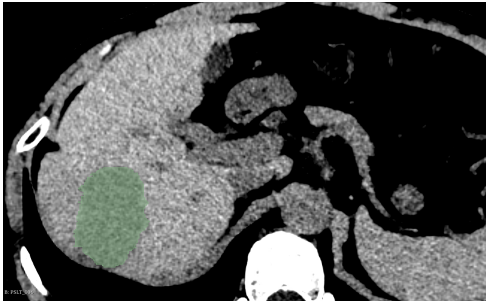
### 3.2.2 | Transformer vs CNN

To validate the efficacy of the transformer module in feature extraction, we conducted a series of comparative experiments. We experimented with substituting both branches of the dual-encoder architecture entirely with CNN architectures. This configuration yielded an accuracy of 57.35%. By contrast, utilizing the transformer for extracting low-frequency features and CNNs for high-frequency information, we achieved an accuracy of 60.97%. Conversely, employing CNNs for low-frequency and transformers for high-frequency feature extraction resulted in an accuracy of 59.04%. Both configurations fell short of the 62.63% accuracy attained when transformers were used exclusively in both branches. These results underscore the superiority of transformers in extracting both low and high-frequency information. The ablation study results are visually presented in Table 5 for an intuitive comparison.

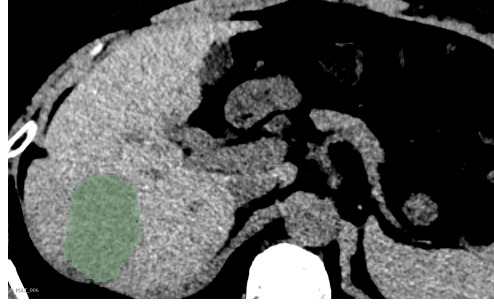
Modules	Dice Coefficient (%)
Two encoders with CNN	57.35
LF(CNN) and HF(16 patches transformer)	59.04
LF(16 patches transformer) and HF(CNN)	60.97
Two encoders with 32 patches transformer	61.08
<b>Two encoders with 16 patches transformer</b>	<b>62.63</b>

**TABLE 5** Ablation experiments

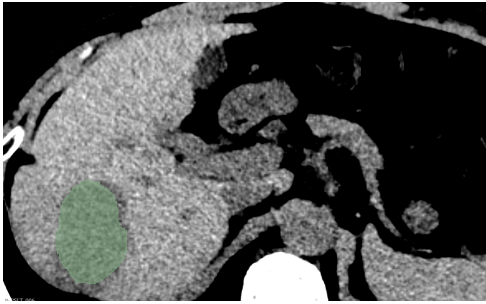




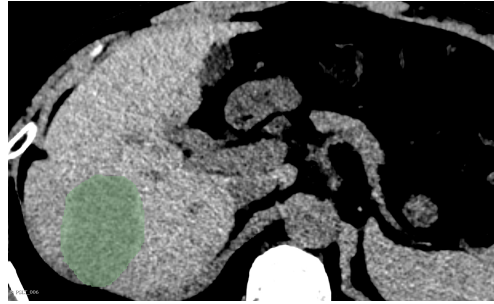
(a) True ground



(b) YNetr



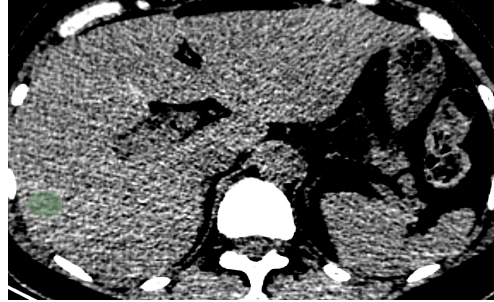
(c) MedNext(3d fullres)



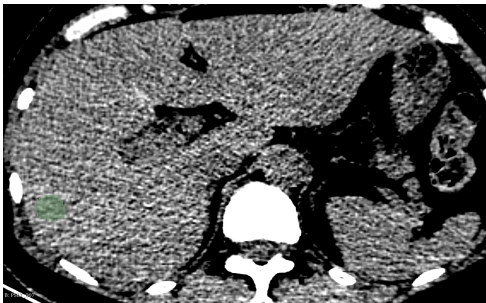
(d) UNetr(baseline)



(e) True ground



(f) YNetr



(g) MedNext(3d fullres)



(h) UNetr(baseline)

First example

Second example

**FIGURE 7** Visualization of 2 randomly selected patients

### 3.2.3 | Loss

**TABLE 6** Segmentation Accuracy of Different Loss Functions

Loss Function	Dice Coefficient (%)
Dice Loss	62.54
Cross-Entropy Loss	62.36
Boundary Loss	62.24
<b>Dice-CE Loss</b>	<b>62.63</b>

In the ablation studies, we evaluated the impact of different loss functions on the performance of our proposed model as Table 6 shows. We considered several commonly used loss functions in medical image segmentation, including Dice Loss, Cross-Entropy (CE) Loss, a combination of Dice and CE Loss (Dice-CE), and Boundary Loss. The effectiveness of each loss function was measured based on the segmentation accuracy, quantified by the Dice coefficient percentage. Notably, the Dice-CE Loss outperformed the other loss functions, achieving the highest accuracy of **62.63%**. This superior performance can be attributed to the balanced combination of Dice and CE Loss. The Dice component of the loss function effectively handles the issue of class imbalance prevalent in medical image datasets, particularly in cases where the region of interest occupies a small portion of the image. Meanwhile, the CE component contributes to robust voxel-wise error penalization, ensuring that each pixel's classification is accurately accounted for. The synergistic effect of combining these two loss functions leads to improved segmentation performance, as evidenced by our experimental results. This underscores the efficacy of the Dice-CE Loss in our task, providing an optimal balance between class imbalance handling and precise voxel-wise classification.

## 4 | DISCUSSION

### 4.1 | Publicly Available Datasets

While extensive research has been conducted on datasets for enhanced CT liver tumor segmentation, there is a notable gap in the literature regarding CT non-contrast datasets for this purpose. Existing field is the LTSC'08 [7] Segmentation Challenge organized by The Cancer Imaging Archive (TCIA), which released 30 enhanced CT voxel datasets specifically for liver tumor segmentation. The LITS [1] dataset from the Technical University of Munich (TUM), consisting of 201 voxel datasets, stands as a benchmark for liver tumor segmentation in enhanced CT imaging.

Complementing these, a variety of datasets from different institutions contribute to the breadth of research in this domain. For example, the TCGA-LIHC [6] dataset from TCIA provides a substantial volume of data with 1,688 instances, although it does not include segmentation labels. The DKFZ institution's SILVER07 [7] dataset presents an additional 30 CT volumes. Siemens and the University of Geneva, with their respective datasets, contribute further to the field, though their focus is not exclusively on liver tumor segmentation. 60 scans with two modalities (MRI and CT) for segmentation and landmark detection in anatomical structure were provided by the VISCERAL taset includes CHAOS [9]with provides 40 CT volumns and 120 MRI volumns. The comparison of these datasets with the PSLT dataset is shown in Table 1.

### 4.2 | Publicly Segmentation Methods

Since the introduction of the UNet [16] architecture, a multitude of semantic segmentation methods based on UNet have been developed, particularly for 3D voxel data. VNet [17], which utilizes 3D CNNs for feature extraction, marked a significant advancement, heralding a new phase in semantic segmentation methods for 3D voxel data. The advent of the vision transformer [4] led to its adoption in various methodologies, such as TransU-Net [18], nn-former [19], CoTr [14], Trans-

BTS [13], Transfuse [20], and UNETR [5], each achieving commendable results. Following the swin transformer's emergence, sliding-window techniques have been implemented in the medical image segmentation field, with swin UNETR [12] showing impressive efficacy across multiple datasets. Later, To make the model more lightweight, Slim UNETR [21] has been proposed. The introduction of nnUNet [2] and mednext [15] provided a significant boon for those less proficient in AI. These systems, through high-level integration and data augmentation, have demonstrated strong performance in numerous tasks. In 2023, XNet was proposed, a novel approach that extracts features from datasets at varying frequencies and employs two branches each for the encoder and decoder. This methodology has achieved state-of-the-art results in a wide range of semi-supervised and fully supervised semantic segmentation tasks.

### 4.3 | Publicly Wavelet-Based for Semantic Segmentation

Incorporating the wavelet transform, renowned for its exceptional frequency and spatial analysis capabilities, into Deep Neural Networks (DNNs) has seen various explorations for semantic segmentation tasks, as evidenced in research works [22, 23, 24, 25, 26, 27]. The primary approaches involve leveraging the wavelet transform for either pre-processing or post-processing tasks [22, 23], as well as substituting specific convolutional neural network (CNN) layers (notably those responsible for up-sampling and down-sampling) with wavelet-based operations [24, 26]. Despite these advancements, the applicability of these methods tends to be confined to particular types of segmentation targets, thereby constraining their widespread utility. A study [28] introduced a symmetric CNN architecture augmented with wavelet transform, named Aerial LaneNet, aimed at enhancing lane-marking semantic segmentation in aerial images. Additionally, the concept of wavelet constrained pooling layers, as an alternative to traditional pooling mechanisms for the segmentation of synthetic aperture radar imagery, was presented

in CWNN [29]. Furthermore, WaveSNet [30] employs wavelet transforms for the meticulous extraction of image nuances during the down-sampling phase and utilizes the inverse wavelet transform to restore these details in the up-sampling process.

### 4.4 | Advantages of Plain Computed Tomography

The advantages of plain computed tomography (CT) over contrast-enhanced CT (CECT) are primarily evident in several key aspects:

- **Reduced harm:** plain scan CT are more convenient because they do not require the injection of contrast media, thus avoiding the associated complications such as contrast media extravasation, allergy and nephropathy. In contrast, CECT requires contrast injection. Iodinated contrast media (ICM) is one of the most frequently administered [31], AKI is a potential complication of intravascular iodinated contrast exposure, which usually presents as a transient small decrease in renal function that occurs within a few days of contrast administration and is associated with serious adverse outcomes, including progressive renal dysfunction and death [32]. It occurs in more than 30% of patients after intravenous iodinated contrast media and causes serious complications [33]. Intravenous administration of a contrast agent is required to assess blood flow to the lesion, and this may cause harm.
- **Time-efficient:** Plain CT scanning is a time-efficient, single-step procedure, and rapid imaging equipment can complete the process in seconds, making it more acceptable to non-compliant patients. This minimizes the patient's exposure to ionizing radiation. For example, While minimizing radiation exposure, ultra-low dose (ULD) CT could facilitate the clinical implementation of large-scale lung cancer screening [34]. However, CECT tends to be lengthier than other imaging techniques due to multiple scanning phases, including non-contrast, arterial, venous, and sometimes delayed phases. This poses greater challenges

for non-compliant patients, increases exposure time, and results in higher radiation doses, which can lead to greater potential harm.

- **Low cost** Cost considerations indicate that plain scan CT are less expensive than CECT. This is because plain CT only involves the fee for the CT procedure itself, whereas CECT involves the fee for the enhanced scan and the contrast agent.
- **Early screening:** plain scan CT are more suitable for screening during health check-ups, as they are generally more acceptable to routine patients than CECT. Whole-body CT enables the identification of a significant number of relevant and early findings, which increase significantly with age, leading to changes in lifestyle and early treatment [35].

## 5 | CHALLENGES

Challenges in lesion identification with plain scan CT include:

plain scan CT cannot accurately assess vascular anomalies such as aneurysms, embolisms, or aortic dissections without contrast media. Lesions may not be discernibly contrasted against surrounding normal tissue, which hinders the ability to display the lesion's structure and internal composition. This limitation can lead to imprecise assessments of lesion size, location, and type, increasing the risk of missed diagnoses or misdiagnoses. Low contrast resolution can make it challenging to differentiate between various structures, such as necrotic or cystic changes, and to detect small pathologies like lesions. In addition, plain scan CT do not allow observation of vascular features, contrast uptake patterns and relationships with surrounding structures, which are necessary to characterize some lesions and therefore CECT is often required for accurate diagnosis. This leads to less comprehensive information, which hinders the conclusive diagnosis and differentiation of benign or malignant lesions. This is not only a diagnostic challenge for the physician, but also a challenge for the artificial intelligence in the segmentation of the lesions in the plain scans. Besides, Large-scale clinical

and imaging modalities, particularly radiological features of contrast-enhanced CT, can be integrated to predict the clinical prognosis of patients with microvascular invasion (MVI) and hepatocellular carcinoma (HCC) [36]. For this reason, we recommend that further research be conducted into the cost-effective segmentation of liver tumors on plain scans.

In conclusion, while identifying liver tumors in plain scans may be more challenging than in contrast-enhanced imaging, the benefits of lower duration, cost, and reduced harm position the segmentation of liver tumors in plain scans as a promising research area. Pre-operative CT features can be used to characterize the macrotrabecular-massive subtype and the vessels that encapsulate tumor clusters pattern. These features have prognostic significance for early recurrence in patients with hepatocellular carcinoma [37].

## 6 | CONCLUSION AND FUTURE WORK

In the segmentation of liver tumors, there is a significant density difference between plain and enhanced CT scans. Compared to enhanced CT, plain CT scans are more challenging to discern. To overcome this difficulty, using wavelet transform to capture varying density information is a good approach. However, determining the most suitable density information and methods for information fusion still requires further research. Additionally, since our PSLT dataset contains only 40 volumes of liver tumor annotations, expanding the dataset and annotating other abdominal regions also necessitates further study.

In conclusion, this paper presents the YNetr model, which employs a dual-transformer architecture as the encoder, tested on the first non-contrast liver tumor segmentation dataset PSLT, achieving state-of-the-art (SOTA) results. In summary, our work not only introduces the inaugural non-contrast liver tumor segmentation dataset for medical research, providing a benchmark accuracy for subsequent studies but also adopts a dual-encoder approach to fuse information across differ-

ent frequencies, offering researchers novel insights into feature extraction methodologies.

## Author Contributions

Wen Sheng: Data management and audit; writing – original draft. Zhong Zheng: Data annotation. Jiajun Liu: Replicate parts of the model and visualization. Han Lu: Replicate parts of the model. Hanyuan Zhang: Replicate parts of the model. Zhengyong Jiang: Funding acquisition; investigation; Writing - review and editing. Zhihong Zhang: Investigation; Data management. Daoping Zhu: Data collection.

## Funding Information

This research was funded by the Suzhou Science and Technology Project (SYG202122), the Research Development Fund of XJTLU (RDF-19-02-23) and Suzhou Municipal Key Laboratory for Intelligent Virtual Engineering (SZS2022004).

## Conflict of Interest Statement

The authors declare no potential conflicts of interest.

## Data Availability Statement

We will upload the datasets into github after being accepted.

## Ethics Statement

This retrospective study was approved by Biological and Medical Ethics Committee of Gong'an County People's Hospital.

## references

- [1] Bilic P, Christ P, Li HB, Vorontsov E, Ben-Cohen A, Kaissis G, et al. The liver tumor segmentation benchmark (lits). *Medical Image Analysis* 2023;84:102680.
- [2] Isensee F, Jaeger PF, Kohl SA, Petersen J, Maier-Hein KH. nnU-Net: a self-configuring method for deep learning-based biomedical image segmentation. *Nature methods* 2021;18(2):203–211.
- [3] Zhou Y, Huang J, Wang C, Song L, Yang G. XNet: Wavelet-Based Low and High Frequency Fusion Networks for Fully-and Semi-Supervised Semantic Segmentation of Biomedical Images. In: *Proceedings of the IEEE/CVF International Conference on Computer Vision*; 2023. p. 21085–21096.
- [4] Dosovitskiy A, Beyer L, Kolesnikov A, Weissenborn D, Zhai X, Unterthiner T, et al. An image is worth 16x16 words: Transformers for image recognition at scale. *arXiv preprint arXiv:201011929* 2020;.
- [5] Hatamizadeh A, Tang Y, Nath V, Yang D, Myronenko A, Landman B, et al. Unetr: Transformers for 3d medical image segmentation. In: *Proceedings of the IEEE/CVF winter conference on applications of computer vision*; 2022. p. 574–584.
- [6] Erickson B, Kirk S, Lee Y, Bathe O, Kearns M, Gerdes C, et al. Radiology data from the cancer genome atlas liver hepatocellular carcinoma [TCGA-LIHC] collection. *Cancer Imaging Arch* 2016;10:K9.
- [7] Heimann T, Van Ginneken B, Styner MA, Arzhaeva Y, Aurich V, Bauer C, et al. Comparison and evaluation of methods for liver segmentation from CT datasets. *IEEE transactions on medical imaging* 2009;28(8):1251–1265.
- [8] Jimenez-del Toro O, Müller H, Krenn M, Gruenberg K, Taha AA, Winterstein M, et al. Cloud-based evaluation of anatomical structure segmentation and landmark detection algorithms: VISCERAL anatomy benchmarks. *IEEE transactions on medical imaging* 2016;35(11):2459–2475.
- [9] Kavur AE, Gezer NS, Barış M, Aslan S, Conze PH, Groza V, et al. CHAOS challenge-combined (CT-MR) healthy abdominal organ segmentation. *Medical Image Analysis* 2021;69:101950.
- [10] Fedorov A, Beichel R, Kalpathy-Cramer J, Finet J, Fillion-Robin JC, Pujol S, et al. 3D Slicer as an image computing platform for the Quantitative Imaging Network. *Magnetic resonance imaging* 2012;30(9):1323–1341.
- [11] Huang H, Lin L, Tong R, Hu H, Zhang Q, Iwamoto Y, et al. Unet 3+: A full-scale connected unet for medical image segmentation. In: *ICASSP 2020-2020 IEEE international conference on acoustics, speech and signal processing (ICASSP) IEEE*; 2020. p. 1055–1059.

- [12] Hatamizadeh A, Nath V, Tang Y, Yang D, Roth HR, Xu D. Swin unetr: Swin transformers for semantic segmentation of brain tumors in mri images. In: International MICCAI Brainlesion Workshop Springer; 2021. p. 272–284.
- [13] Wang W, Chen C, Ding M, Yu H, Zha S, Li J. Transbts: Multimodal brain tumor segmentation using transformer. In: Medical Image Computing and Computer Assisted Intervention–MICCAI 2021: 24th International Conference, Strasbourg, France, September 27–October 1, 2021, Proceedings, Part I 24 Springer; 2021. p. 109–119.
- [14] Xie Y, Zhang J, Shen C, Xia Y. Cotr: Efficiently bridging cnn and transformer for 3d medical image segmentation. In: Medical Image Computing and Computer Assisted Intervention–MICCAI 2021: 24th International Conference, Strasbourg, France, September 27–October 1, 2021, Proceedings, Part III 24 Springer; 2021. p. 171–180.
- [15] Roy S, Koehler G, Ulrich C, Baumgartner M, Petersen J, Isensee F, et al. Mednext: transformer-driven scaling of convnets for medical image segmentation. In: International Conference on Medical Image Computing and Computer-Assisted Intervention Springer; 2023. p. 405–415.
- [16] Ronneberger O, Fischer P, Brox T. U-net: Convolutional networks for biomedical image segmentation. In: Medical Image Computing and Computer-Assisted Intervention–MICCAI 2015: 18th International Conference, Munich, Germany, October 5–9, 2015, Proceedings, Part III 18 Springer; 2015. p. 234–241.
- [17] Milletari F, Navab N, Ahmadi SA. V-net: Fully convolutional neural networks for volumetric medical image segmentation. In: 2016 fourth international conference on 3D vision (3DV) Ieee; 2016. p. 565–571.
- [18] Chen J, Lu Y, Yu Q, Luo X, Adeli E, Wang Y, et al. Transunet: Transformers make strong encoders for medical image segmentation. arXiv preprint arXiv:210204306 2021;.
- [19] Zhou HY, Guo J, Zhang Y, Yu L, Wang L, Yu Y. nnformer: Interleaved transformer for volumetric segmentation. arXiv preprint arXiv:210903201 2021;.
- [20] Zhang Y, Liu H, Hu Q. Transfuse: Fusing transformers and cnns for medical image segmentation. In: Medical Image Computing and Computer Assisted Intervention–MICCAI 2021: 24th International Conference, Strasbourg, France, September 27–October 1, 2021, Proceedings, Part I 24 Springer; 2021. p. 14–24.
- [21] Pang Y, Liang J, Huang T, Chen H, Li Y, Li D, et al. Slim UNETR: Scale Hybrid Transformers to Efficient 3D Medical Image Segmentation Under Limited Computational Resources. IEEE Transactions on Medical Imaging 2023;.
- [22] Yin X, Xu X. A Method for Improving Accuracy of DeepLabv3+ Semantic Segmentation Model Based on Wavelet Transform. In: International Conference in Communications, Signal Processing, and Systems Springer; 2021. p. 315–320.
- [23] Upadhyay K, Agrawal M, Vashist P. Wavelet based fine-to-coarse retinal blood vessel extraction using Unet model. In: 2020 International Conference on Signal Processing and Communications (SPCOM) IEEE; 2020. p. 1–5.
- [24] Zhao C, Xia B, Chen W, Guo L, Du J, Wang T, et al. Multi-scale wavelet network algorithm for pediatric echocardiographic segmentation via hierarchical feature guided fusion. Applied Soft Computing 2021;107:107386.
- [25] Sinha P, Wu Y, Psaromiligkos I, Zilic Z. Lumen & media segmentation of IVUS images via ellipse fitting using a wavelet-decomposed subband CNN. In: 2020 IEEE 30th International Workshop on Machine Learning for Signal Processing (MLSP) IEEE; 2020. p. 1–6.
- [26] Gao F, Wang X, Gao Y, Dong J, Wang S. Sea ice change detection in SAR images based on convolutional-wavelet neural networks. IEEE Geoscience and Remote Sensing Letters 2019;16(8):1240–1244.
- [27] Liu P, Zhang H, Lian W, Zuo W. Multi-level wavelet convolutional neural networks. IEEE Access 2019;7:74973–74985.
- [28] Azimi SM, Fischer P, Körner M, Reinartz P. Aerial LaneNet: Lane-marking semantic segmentation in aerial imagery using wavelet-enhanced cost-sensitive symmetric fully convolutional neural networks. IEEE Transactions on Geoscience and Remote Sensing 2018;57(5):2920–2938.
- [29] Duan Y, Liu F, Jiao L, Zhao P, Zhang L. SAR image segmentation based on convolutional-wavelet neural network and Markov random field. Pattern Recognition 2017;64:255–267.

- 
- [30] Li Q, Shen L. Wavesnet: Wavelet integrated deep networks for image segmentation. In: Chinese Conference on Pattern Recognition and Computer Vision (PRCV) Springer; 2022. p. 325–337.
- [31] Macdonald DB, Hurrell CD, Costa AF, McInnes MD, O'Malley M, Barrett BJ, et al. Canadian association of radiologists guidance on contrast-associated acute kidney injury. *Canadian Journal of Kidney Health and Disease* 2022;9:20543581221097455.
- [32] Cashion W, Weisbord SD. Radiographic contrast media and the kidney. *Clinical Journal of the American Society of Nephrology* 2022;17(8):1234–1242.
- [33] Lin Q, Li S, Jiang N, Shao X, Zhang M, Jin H, et al. PINK1-parkin pathway of mitophagy protects against contrast-induced acute kidney injury via decreasing mitochondrial ROS and NLRP3 inflammasome activation. *Redox biology* 2019;26:101254.
- [34] Jiang B, Li N, Shi X, Zhang S, Li J, de Bock GH, et al. Deep learning reconstruction shows better lung nodule detection for ultra-low-dose chest CT. *Radiology* 2022;303(1):202–212.
- [35] Millor M, Bartolomé P, Pons MJ, Bastarrika G, Beloqui Ó, Cano D, et al. Whole-body computed tomography: a new point of view in a hospital check-up unit? Our experience in 6516 patients. *La radiologia medica* 2019;124:1199–1211.
- [36] Xu X, Zhang HL, Liu QP, Sun SW, Zhang J, Zhu FP, et al. Radiomic analysis of contrast-enhanced CT predicts microvascular invasion and outcome in hepatocellular carcinoma. *Journal of hepatology* 2019;70(6):1133–1144.
- [37] Feng Z, Li H, Zhao H, Jiang Y, Liu Q, Chen Q, et al. Preoperative CT for characterization of aggressive macrotrabecular-massive subtype and vessels that encapsulate tumor clusters pattern in hepatocellular carcinoma. *Radiology* 2021;300(1):219–229.